

PAPER • OPEN ACCESS

Time-resolved quantum process tomography using Hamiltonian-encoding and observable-decoding

To cite this article: Roberto Rey-de-Castro *et al* 2013 *New J. Phys.* **15** 025032

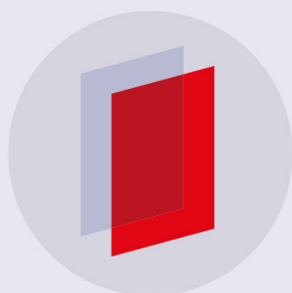
View the [article online](#) for updates and enhancements.

Related content

- [Control of quantum phenomena: past, present and future](#)
Constantin Brif, Raj Chakrabarti and Herschel Rabitz
- [A stochastic approach to open quantum systems](#)
R Biele and R D'Agosta
- [Dynamics of the reading process of a quantum memory](#)
Milrian S Mendes, Pablo L Saldanha, José W R Tabosa *et al.*

Recent citations

- [Gaining Mechanistic Insight with Control Pulse Slicing: Application to the Dissociative Ionization of CH₂BrI](#)
Xi Xing *et al*
- [Identifying different mechanisms in the control of a nitrogen–vacancy center system](#)
Shouzhi Li *et al*
- [Estimation of a general time-dependent Hamiltonian for a single qubit](#)
L. E. de Clercq *et al*



IOP | ebooks™

Bringing you innovative digital publishing with leading voices to create your essential collection of books in STEM research.

Start exploring the collection - download the first chapter of every title for free.

Time-resolved quantum process tomography using Hamiltonian-encoding and observable-decoding

Roberto Rey-de-Castro¹, Renan Cabrera, Denys I Bondar
and Herschel Rabitz

Department of Chemistry, Princeton University, Princeton, NJ 08544, USA
E-mail: rrey@princeton.edu

New Journal of Physics **15** (2013) 025032 (21pp)

Received 10 July 2012

Published 25 February 2013

Online at <http://www.njp.org/>

doi:10.1088/1367-2630/15/2/025032

Abstract. The Hamiltonian encoding observable decoding (HE-OD) technique is experimentally demonstrated for process tomography of laser-induced dynamics in atomic Rb vapor. With the assistance of a laser pulse truncation method, a time dependent reconstruction of the quantum evolution is achieved. HE-OD can perform full as well as partial process tomography with appropriate measurements to characterize the system. The latter feature makes HE-OD tomography suitable for analyzing quantum processes in complex systems.

¹ Author to whom any correspondence should be addressed.



Content from this work may be used under the terms of the [Creative Commons Attribution-NonCommercial-ShareAlike 3.0 licence](https://creativecommons.org/licenses/by-nc-sa/3.0/). Any further distribution of this work must maintain attribution to the author(s) and the title of the work, journal citation and DOI.

Contents

1. Introduction	2
2. Theoretical background	3
2.1. Hamiltonian encoding observable decoding (HE-OD)	3
2.2. Time-resolved HE-OD	6
2.3. Dynamical transition widths	7
2.4. Application to atomic Rb	8
2.5. Rabi flopping	12
3. Experimental implementation	13
3.1. Experimental setup	13
3.2. Encoding	13
3.3. Field truncation	14
3.4. Time-resolved modulated signal	16
3.5. Decoding	16
3.6. Extracted pathway ratios	17
4. Future prospects for HE-OD tomography	19
Acknowledgments	20
Appendix	20
References	21

1. Introduction

Quantum tomography is a diverse field of research directed toward extracting quantum states [1–4], processes [3, 5–8], and Hamiltonians [9, 10]. Considering the needs of quantum computation, communication, and metrology, most efforts have focused on complete state/process reconstruction at a fixed time. However, such approaches designed for extracting full information are demanding on the quantity and quality of experimental measurements [4] and generally do not scale well with system complexity. There are a number of important situations (e.g. dynamics in photosynthesis, plasmas, nano systems, etc) when all the required measurements needed to completely characterize the quantum dynamics are not feasible to perform; thus, extracting well defined partial system information would be desirable, but this goal is difficult to achieve by traditional quantum tomography methods. Motivated by these challenges, the Hamiltonian encoding observable decoding (HE-OD) [11, 12] technique was recently developed to allow for full as well as partial reconstruction of quantum dynamics driven by a laser field.

The foundations of HE-OD can be appreciated by considering state-to-state population transfer. Given multiple pathways connecting the final and initial states, the population in the final state arises from quantum mechanical interference, which is sensitive to the relative phase of the amplitude associated with each pathway. Since the transitions are induced by an applied laser pulse, the relative phases in the pulse at the frequencies driving the transitions affect the pathway amplitudes, thereby controlling the final state population. HE-OD provides a general methodology for reconstructing the complex-valued pathway amplitudes by measuring the populations' dependence on the laser phases (details are given in section 2). In contrast with standard quantum process tomography, HE-OD is based on performing measurements

sensitive to *selected* pathway amplitudes instead of aiming to estimate the full process matrix (i.e. the map between all possible inputs and all possible outputs). Although it is possible to use HE-OD to obtain the amplitudes of all the participating pathways, HE-OD is most useful as a systematic procedure for extracting selected pathway amplitudes of interest, therefore focusing the effort only where it is needed. Another attractive feature of HE-OD is that it requires minimal alteration to the experimental setups already available in laboratories with laser pulse shaping capabilities.

After first presenting the foundations of HE-OD, we employ the technique to experimentally retrieve time-dependent process tomographic information from laser induced transitions in gas phase atomic Rb. To achieve temporal resolution of the control process, a novel method for laser pulse truncation is utilized. These experiments also provide the basis for performing partial dynamical tomography of quantum processes in complex systems.

The paper is structured as follows. Section 2 contains a detailed presentation of HE-OD for time-resolved reconstruction of multiple pathway amplitudes. In section 3, we describe HE-OD's experimental implementation for partial tomography of laser induced dynamics in Rb. Concluding remarks are presented in section 4.

2. Theoretical background

2.1. Hamiltonian encoding observable decoding (HE-OD)

We present the HE-OD technique for a N -level quantum system undergoing unitary dynamics driven by a laser field $E(t)$ [13]. The system's Hamiltonian is considered to be of the form $H = H_0 - \mu E(t)$, where H_0 is the unperturbed Hamiltonian with eigenvalues ϵ_n and eigenstates $|n\rangle$ ($n = 1, 2, \dots, N$), and μ denotes the dipole moment operator. The system dynamics are governed by the evolution operator $U(t)$ satisfying the time-dependent Schrödinger equation in the interaction representation:

$$i\hbar \frac{dU(t)}{dt} = V_I(t)U(t), \quad (1)$$

where

$$V_I(t) = -\exp\left(-\frac{i}{\hbar}H_0t\right)\mu\exp\left(\frac{i}{\hbar}H_0t\right)E(t) \quad (2)$$

and $U(0) = I$. The solution of equation (1) can be expressed in terms of the Dyson expansion [14]

$$U(T) = I + \left(\frac{-i}{\hbar}\right) \int_0^T V_I(t_1)dt_1 + \left(\frac{-i}{\hbar}\right)^2 \int_0^T V_I(t_2) \int_0^{t_2} V_I(t_1)dt_1 dt_2 + \dots, \quad (3)$$

where T is the time when an observation is performed. The convergence of the series in equation (3) in the case of realistic pulses can be readily established [11]. The HE-OD formalism can be applied to the expectation value of any observable operator O [12] given by $\langle O \rangle = \text{Tr}(\rho O)$, where ρ is the density matrix of the system. For clarity, we treat the particular case of a system undergoing unitary evolution with $\rho(0) = |a\rangle\langle a|$ and $O = |b\rangle\langle b|$. In this circumstance $\langle O(T) \rangle = |U_{ba}(T)|^2$, with $U_{ba}(T) = \langle a|U(T)|b\rangle$. After identifying a control field (optimal or otherwise), the first step in HE-OD is to *encode* the field and thus the dynamics. To understand

the role of encoding in HE-OD, consider the expansion of the population transfer amplitude from equation (3)

$$U_{ba}(T) = \sum_{n, \{l_i\}} U_{ba}^{n(l_1, l_2, \dots, l_{n-1})}(T), \quad (4)$$

where

$$U_{ba}^{n(l_1, l_2, \dots, l_{n-1})}(T) = \left(\frac{-i}{\hbar}\right)^n \int_0^T \mu_{bl_{n-1}} e^{-i\omega_{bl_{n-1}} t_n} E(t_n) \int_0^{t_n} \mu_{l_{n-1}l_{n-2}} e^{-i\omega_{l_{n-1}l_{n-2}} t_{n-1}} E(t_{n-1}) \int_0^{t_{n-1}} \dots \times \dots \int_0^{t_3} \mu_{l_2 l_1} e^{-i\omega_{l_2 l_1} t_2} E(t_2) \int_0^{t_2} \mu_{l_1 a} e^{-i\omega_{l_1 a} t_1} E(t_1) dt_1 dt_2 \dots dt_{n-1} dt_n, \quad (5)$$

with $\omega_{jk} = (\epsilon_j - \epsilon_k) / \hbar$, and $\mu_{jk} = \langle j | \mu | k \rangle$. Equation (5) gives the pathway amplitude $U_{ba}^{n(l_1, l_2, \dots, l_{n-1})}(T)$ for the transition from $|a\rangle$ to $|b\rangle$ through a sequence of n steps $|a\rangle \rightarrow |l_1\rangle \rightarrow |l_2\rangle \rightarrow \dots \rightarrow |l_{n-1}\rangle \rightarrow |b\rangle$, which constitutes one of many possible n th order pathways for the quantum system to reach state $|b\rangle$ from state $|a\rangle$. In the present analysis, $|a\rangle$, $|b\rangle$, and $\{|l_i\rangle\}$ are all considered as eigenstates of H_0 ; the same analysis follows for other bases, but the choice of $\{|l_i\rangle\}$ can alter the physical interpretation of the pathway amplitudes extracted from the experiments. The goal of HE-OD in this context is to perform tailored experiments (i.e. by encoding the field and then decoding of the measurements) to extract the pathway amplitudes in equation (4).

The encoding in HE-OD can be done by introducing phases into selected spectral components of the input field $E(t)$, which may be accomplished in the laboratory by a pulse shaper [12]. The process requires a sequence of m experiments in which the added phases take on distinct values. Consider a field $E(t)$ of the form

$$E(t) = C_0(t)e^{i\omega_0 t} + \sum_{k=1}^M C_k(t)e^{i\omega_k t} + \text{c.c.},$$

where C_0, \dots, C_M are slowly varying functions of time, ω_0 is the ultrafast pulse carrier frequency, and the M selected frequencies $\omega_k \neq 0$ are within the laser bandwidth. Now consider an encoded field $E_s(t)$ of the form

$$E_s(t) = C_0(t)e^{i\omega_0 t} + \sum_{k=1}^M C_k(t)e^{i(\omega_k t + f_k(s))} + \text{c.c.}, \quad (6)$$

where we have added a phase $f_k(s)$ to each field frequency component ω_k , $k = 1, \dots, M$, and each phase $f_k(s)$ is a function of the encoding variable s . In practice, freedom exists to encode any portion of the field as implied by equation (6), where $C_0(t)$ is now understood to include all un-encoded frequency components. This versatility is an important feature for extracting partial tomographic information in complex systems.

If the frequencies ω_k for $k = 1, \dots, M$ (where the encoding is applied) are tuned close to the transition frequencies, e.g. $\omega_{ll'}$ corresponding to the $|l\rangle \rightarrow |l'\rangle$ transition, then inserting the encoded field of equation (6) into equation (5) and keeping only the resonant terms in the integrands, gives a modulated pathway amplitude of the form

$$U_{ba}^{n(l_1, l_2, \dots, l_{n-1})}(s, T) = \exp\left[i \sum_{k=1}^M n_k f_k(s)\right] \times U_{ba}^{n(l_1, l_2, \dots, l_{n-1})}(T), \quad (7)$$

where n_k represents the number of occurrences of transitions with energies close to $\hbar\omega_k$ in the pathway $|a\rangle \rightarrow |l_1\rangle \rightarrow |l_2\rangle \rightarrow \dots \rightarrow |l_{n-1}\rangle \rightarrow |b\rangle$.

Let $\{n\}$ denote the M -tuple of integers n_1, \dots, n_M . A modulating function of s is defined as

$$h(\{n\}; s) \equiv \exp \left[i \sum_{k=1}^M n_k f_k(s) \right]. \quad (8)$$

The effects of encoding are clearly seen in equation (7), where each original pathway amplitude $U_{ba}^{n(l_1, l_2, \dots, l_{n-1})}(T)$ is multiplied by the function $h(\{n\}; s)$. Several pathways may have the same $\{n\}$, i.e. there may be more than one pathway crossing n_k -times through transitions with energies close to $\hbar\omega_k$ for $k = 1, \dots, M$. For example, if transitions $|1\rangle \rightarrow |5\rangle$ and $|5\rangle \rightarrow |9\rangle$ are encoded with $f_1(s)$ and $f_2(s)$, respectively, then pathway $|1\rangle \rightarrow |5\rangle \rightarrow |9\rangle$ will have the same modulation $\exp i[f_1(s) + f_2(s)]$ as $|1\rangle \rightarrow |5\rangle \rightarrow |1\rangle \rightarrow |5\rangle \rightarrow |9\rangle$, since the modulating functions cancel out (i.e. $f_1(s) - f_1(s) = 0$) in the intermediate step $|5\rangle \rightarrow |1\rangle \rightarrow |5\rangle$. In the following, all the transitions collectively modulated by the same function $h(\{n\}; s)$ will have their amplitudes added together to form a *composite* pathway amplitude $U_{ab}^{\{n\}}(T)$ [11].

In terms of composite pathways, the total modulated transition amplitude can be compactly written as

$$U_{ba}(s, T) = \sum_{\{n\}} h(\{n\}; s) \times U_{ba}^{\{n\}}(T). \quad (9)$$

The goal of HE-OD in this context is to find the set of composite pathway amplitudes $U_{ab}^{\{n\}}(T)$ [11] that are above the noise level. As an illustration, the observable considered here is the population transfer given by

$$\begin{aligned} \langle O(s, T) \rangle &= |U_{ba}(s, T)|^2 \\ &= \sum_{\substack{\{n\} \\ \{n'\}}} h(\{n\} - \{n'\}; s) \times U_{ba}^{\{n\}}(T) U_{ba}^{\{n'\}*}(T). \end{aligned}$$

A series of experiments are performed to obtain $\langle O(s, T) \rangle$ as a function of s . In practice s will be discretized to have integer values $s = 1, \dots, m$ (see section A.1) which label the sequence of encoded experiments. To find the pathways contributing to $\langle O(s, T) \rangle$, we define the scalar product between two functions of the set as

$$h(\{n\}; s) \circ h(\{n'\}; s) \equiv \frac{1}{N} \sum_{s=1}^m h(\{n\}; s) \times h^*(\{n'\}; s), \quad \forall \{n\}, \{n'\}. \quad (10)$$

If the encoding functions $f_k(s)$, $k = 1, \dots, M$ are chosen such that all members of the set $\{h(\{n\}; s), \forall \{n\}\}$ are orthonormal (see section A.1), then $\langle O(s, T) \rangle$ produces well defined relations between the pathway amplitudes and projections $P(\{\tilde{n}\}; T)$ that can be extracted from the data as

$$P(\{\tilde{n}\}; T) \equiv \langle O(s, T) \rangle \circ h(\{\tilde{n}\}; s) \quad (11)$$

$$= \sum_{\substack{\{n\} \\ \{n'\}}} h(\{n\} - \{n'\}; s) \circ h^*(\{\tilde{n}\}; s) \times U_{ba}^{\{n\}}(T) U_{ba}^{\{n'\}*}(T), \quad (12)$$

$$= \sum_{\{n\}} U_{ba}^{\{n\}}(T) U_{ba}^{\{n\} - \{\tilde{n}\}*}(T). \quad (13)$$

Since the projections $P(\{\tilde{n}\}; T)$ can be experimentally evaluated by first measuring $\langle O(s, T) \rangle$ and then using equation (11), the pathway amplitudes $U_{ba}^{\{n\}}(T)$ may be obtained by solving the system of quadratic algebraic equations (13). In practice, ratios of various projections $P(\{\tilde{n}\}; T)$ can suffice to give desired process tomography information.

2.2. Time-resolved HE-OD

The temporal evolution of the amplitudes $U_{ba}^{\{n\}}(T)$ may be determined by applying the methods of section 2.1 to measurements of the modulated observable $\langle O(s, T) \rangle$ at varying times T . The expectation value of any observable measured at time T is determined by the evolution operator expansion in equation (3). A measurement at time T is characterized by a truncation at T of all the outer integrals on the right hand side (rhs) of equation (3). For the state-to-state observable treated here an equivalent procedure is to keep the measurement time T constant while truncating the laser field at different times $\tau < T$ [15]. Consider this procedure with a truncated field defined as

$$E(t, \tau) \equiv \begin{cases} E(t), & t \leq \tau, \\ 0, & t > \tau, \end{cases} \quad (14)$$

where $E(t)$ is the unaltered field. Field truncation results in a truncated potential

$$V_I(t, \tau) = -\exp\left(-\frac{i}{\hbar}H_0t\right) \mu \exp\left(\frac{i}{\hbar}H_0t\right) E(t, \tau). \quad (15)$$

Substituting equation (15) into equation (2) and then into equation (3) gives the expansion for the evolution operator $U(T, \tau)$ corresponding to dynamics driven by the truncated field $E(t, \tau)$ and with a measurement performed at time T

$$\begin{aligned} U(T, \tau) &= I + \left(\frac{-i}{\hbar}\right) \int_0^T V_I(t_1, \tau) dt_1 + \left(\frac{-i}{\hbar}\right)^2 \int_0^T V_I(t_2, \tau) \int_0^{t_2} V_I(t_1, \tau) dt_1 dt_2 + \dots \\ &= I + \left(\frac{-i}{\hbar}\right) \int_0^\tau V_I(t_1) dt_1 + \left(\frac{-i}{\hbar}\right)^2 \int_0^\tau V_I(t_2) \int_0^{t_2} V_I(t_1) dt_1 dt_2 + \dots \\ &= U(\tau). \end{aligned} \quad (16)$$

Thus, when the truncated field $E(t, \tau)$ is employed, a measurement of the state-to-state observable O at a time $T > \tau$ yields the same expectation value as the measurement of O at time τ , $\langle O(\tau) \rangle$. The encoded field $E_s(t)$ can be truncated to form $E_s(t, \tau)$ at varying times τ to measure the temporal dependence of $\langle O(s, \tau) \rangle$, which then allows for the extraction of the temporally-resolved pathway amplitudes $U_{ba}^{\{n\}}(\tau)$ using the methods of section 2.1.

A truncated field $E(t, \tau)$ can be obtained by multiplying the original field $E(t)$ by a time-domain step function

$$E(t, \tau) = E(t) \times h(t - \tau), \quad (17)$$

where $h(t) = 1$ for $t \leq 0$, and $h(t) = 0$ for $t > 0$. In the frequency domain

$$E(\omega, \tau) = \int_{-\infty}^{+\infty} E(\omega') \times H_\tau(\omega - \omega') d\omega', \quad (18)$$

where ω is the angular frequency, and $E(\omega)$ and $H_\tau(\omega)$ are the Fourier transforms of $E(t)$ and $h(t - \tau)$, respectively. A sudden truncation of $E(t)$ is experimentally unattainable. A practical

approximation to $E(t, \tau)$ can be produced by rapidly turning-off $E(t)$. In the experiments we used

$$h(t) = \frac{1}{2}\text{erfc}(t/\Delta t), \quad (19)$$

where erfc is the complementary error function, and Δt defines the turn-off time.

In a discrete frequency representation, the truncated field is given by

$$E(\omega_j, \tau) \approx \sum_{k=1}^N E(\omega_k) H_\tau(\omega_j - \omega_k), \quad (20)$$

where N is the number of spectral components. In the laboratory the field is more conveniently represented in terms of wavelength λ

$$E(\lambda_j, \tau) \approx \sum_{k=1}^N E(\lambda_k) H_\tau(\lambda_j - \lambda_k), \quad (21)$$

and the following transformation yields the truncated field $E(\lambda, \tau)$ from the original field $E(\lambda)$:

$$E(\lambda_j, \tau) = M(\lambda_j, \tau) \times E(\lambda_j), \quad (22)$$

where

$$M(\lambda_j, \tau) = \frac{\sum_{k=1}^N E(\lambda_k) H_\tau(\lambda_j - \lambda_k)}{E(\lambda_j)}. \quad (23)$$

Numerical simulations showed that the truncated field $E(t, \tau)$ is very sensitive to the phase but not to the amplitude shape of $E(\lambda)$ (for a constant pulse energy). Equation (23) was employed to calculate spectral masks to experimentally turn off laser fields at desired times τ . A similar procedure for truncating ultrafast laser pulses was introduced in [15].

2.3. Dynamical transition widths

When an ultrafast pulse $E(t) = \int_{\Omega} E(\omega) \cos(\omega t) d\omega$ (where Ω is the field's frequency bandwidth) is employed, spectral components of $E(\omega)$ over a frequency window can contribute to each electronic transition, which cease to be sharp resonances. To see this behavior, consider the first-order amplitude

$$\begin{aligned} U_{ab}(\Delta t) &= \int_0^{\Delta t} \mu_{ab} e^{-i\omega_{ab}t} E(t) dt \\ &= \mu_{ab} \int_{\Omega} E(\omega) G(\omega, \Delta t) d\omega, \end{aligned} \quad (24)$$

where $\omega_{ab} > 0$, and

$$G(\omega, \Delta t) = 2 e^{i(\omega - \omega_{ab})\Delta t/2} \frac{\sin[(\omega - \omega_{ab})\Delta t/2]}{\omega - \omega_{ab}}. \quad (25)$$

The rotating wave approximation was used to obtain equation (25). For long times Δt , $G(\omega, \Delta t)$ approximates the delta function $\delta(\omega - \omega_{ab})$. For short times Δt , it can be seen from equations (24) and (25) that not only ω_{ab} but also other spectral components near ω_{ab} contribute to $U_{ab}(\Delta t)$. Thus, for ultrafast applied fields $E(t)$ there is a relatively broad frequency band

for each atomic electronic transition (typically corresponding to few to tens of nanometers). This behavior adds flexibility to the implementation of HE-OD because the encoding can be applied to the whole transition width or to just a part of it, thereby giving information about how different portions of the transition bandwidth contribute to the composite pathways.

Alternatively, the energy level broadening described here can be viewed as a consequence of the energy–time uncertainty principle. The transitions induced by $E(t)$ have an associated time uncertainty Δt (i.e. the time in which amplitude is transferred from one state to another) with a corresponding energy uncertainty $\Delta\epsilon$. The faster the transition, the smaller is Δt and the larger is $\Delta\epsilon$. This view is related to equations (24) and (25) since the transition widths follow the changes caused by the pulse’s temporal profile, e.g. for $E(t)$ corresponding to a multi-pulse sequence, there is a Δt associated with each pulse of the sequence, since for a sequence of well separated pulses the integral in equation (24) can be separated into a summation of integrals whose integrands take significant values at different times. Similar effects will be induced by more complex field shapes. As a consequence, the field $E(t)$ can exert control over the temporal evolution of the energy level widths through the shape of its frequency–time profile. For instance, the field may have a large part of its bandwidth concentrated at certain times, inducing fast population transfers over selected transitions, which we consequently refer to as ‘widening’ of the energy levels involved at those times.

2.4. Application to atomic Rb

The energy level diagram for atomic Rb is shown in figure 1. The Rb states of interest are the five energy eigenstates $|k\rangle$, $k = 1, \dots, 5$. After laser pulse excitation, the final population of level $|4\rangle$ decays to level $|O\rangle$ emitting the observed 421.55 nm fluorescence. This fluorescence is the observable signal $\langle O(T) \rangle$, which is proportional to the population of $|4\rangle$ at the measurement time T long after the excitation pulse $E(t)$ is over

$$\langle O(T) \rangle \propto |U_{41}(T)|^2. \quad (26)$$

From equations (4) and (5) as well as the fact that a minimum of two photons is needed to induce the transition from $|1\rangle$ to $|4\rangle$, $U_{41}(T)$ can be approximated by its two lowest-order expansion terms

$$\langle 4|U(T)|1\rangle = U_1(T) + U_2(T), \quad (27)$$

where

$$U_1(T) = \int_0^T \mu_{42} e^{-i\omega_{42}t_2} E(t_2) \int_0^{t_2} \mu_{21} e^{-i\omega_{21}t_1} E(t_1) dt_1 dt_2, \quad (28)$$

$$U_2(T) = \int_0^T \mu_{43} e^{-i\omega_{43}t_2} E(t_2) \int_0^{t_2} \mu_{31} e^{-i\omega_{31}t_1} E(t_1) dt_1 dt_2, \quad (29)$$

with ω_{jk} and μ_{jk} being the transition frequency and dipole moment between states $|j\rangle$ and $|k\rangle$, for $j, k = 1, \dots, 5$. The experiments were carried out at low intensity such that second-order processes were dominant (see also discussion in section 2.5). The amplitudes U_1 and U_2 represent the double transitions $|1\rangle \rightarrow |2\rangle \rightarrow |4\rangle$ and $|1\rangle \rightarrow |3\rangle \rightarrow |4\rangle$, which are referred to as pathways 1 and 2, respectively, in figure 1(a). Thus, the formulation of section 2.1 can be directly utilized with $\{n\} = n_1, n_2$.

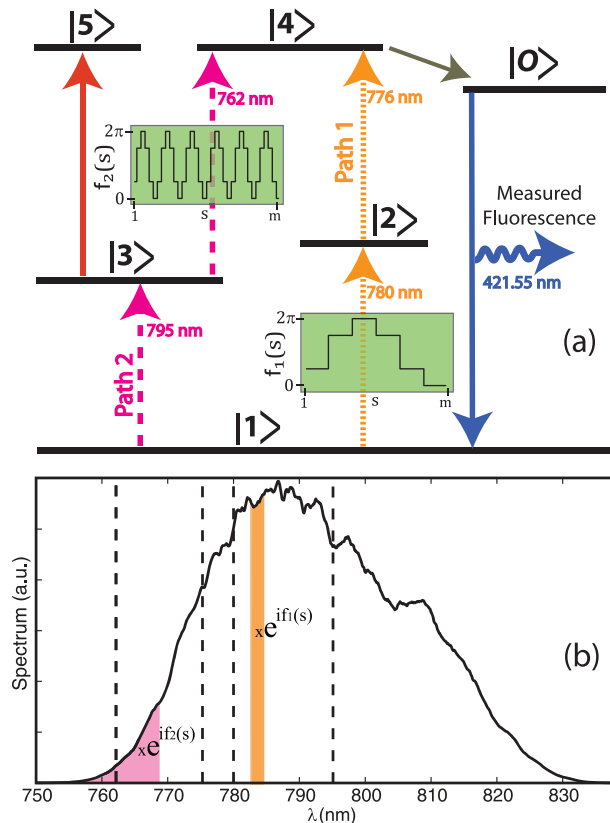


Figure 1. (a) Energy level diagram and transitions for atomic Rb. States $|1\rangle$, $|2\rangle$, $|3\rangle$, $|4\rangle$, $|5\rangle$ and $|O\rangle$ correspond to the levels $5S_{1/2}$, $5P_{1/2}$, $5P_{3/2}$, $5D_{3/2}$, $5D_{5/2}$ and $6P_{1/2}$, respectively. Other Rb states were not reachable at our intensities and due to negligible laser spectral power at and below 740 nm. Initially, only the ground state $|1\rangle$ is populated, and the laser pulse excites the upper levels. After the laser pulse is over, the final population of level $|4\rangle$ decays to level $|O\rangle$ which, in turn, decays back to $|1\rangle$ emitting fluorescence at 421.55 nm. This fluorescence line is measured and taken as the signal $\langle O \rangle$, which is proportional to the final population of state $|4\rangle$. The green-background plots inserted over transitions $|1\rangle \rightarrow |2\rangle$ and $|3\rangle \rightarrow |4\rangle$ illustrate the encoding implemented over m measurements. In measurement s , with $s = 1, 2, \dots, m$, the phases of the spectral components of $E(t)$ around 780 and 762 nm were encoded by adding in $f_1(s)$ and $f_2(s)$ to modulate path 1 (orange-dotted arrows) and path 2 (pink-dashed arrows), respectively. Level $|5\rangle$ is also populated, but it does not contribute to the measured fluorescence, and it can be omitted from the analysis as only second-order pathways are significantly involved. Not shown is the path for fluorescence at 420 nm associated with states $|4\rangle$ and $|5\rangle$. (b) Spectrum of the laser pulse used in the experiments (solid line). The center of the Rb transitions are shown as vertical dashed lines, and the orange and pink areas under the spectrum indicate the position of the encoding. Due to transition overlaps, the encoding over transition $|1\rangle \rightarrow |2\rangle$ was located to the right of the transition center (780 nm) in order to reduce the encoding over the nearby transition $|2\rangle \rightarrow |4\rangle$ (776 nm).

Here we consider an encoding equivalent to the one employed in the experiments described in section 3. There is wide flexibility for choosing the encoding, and practical considerations for Rb dictated the following circumstances. Spectral components close to ω_{21} and ω_{43} were encoded with $f_1(s)$ and $f_2(s)$, respectively. Additionally, the encoding around ω_{43} is wide enough to cover the entire transition width, and the encoding over ω_{21} was chosen much narrower than the encoding over ω_{43} (see figure 1(b)). Thus, the encoded field in equation (6) now has the specific form

$$E_s(t) = e^{i\omega_{42}t} C'_0(t) + e^{i\omega_{31}t} C''_0(t) + e^{i\omega_{21}t} C'''_0(t) + e^{if_1(s)} [e^{i\omega_{21}t} C_1(t) + e^{i\omega_{42}t} C'_1(t) + e^{i\omega_{31}t} C''_1(t)] \\ + e^{if_2(s)} [e^{i\omega_{43}t} C_2(t) + e^{i\omega_{42}t} C'_2(t)] + \text{c.c.}, \quad (30)$$

where $C'_0(t), \dots, C'_2(t)$ are slowly-varying functions. Since the encoding was applied close to ω_{21} and ω_{43} , the encoding over ω_{21} is narrow, and considering as well the spectral profile in figure 1(b), we have

$$C_2(t), C'_0(t), C''_0(t), C'''_0(t) > C_1(t) \gg C'_1(t), C''_1(t), C'_2(t). \quad (31)$$

The terms in equation (30) involving $C'_1(t), C''_1(t)$, and $C'_2(t)$ account for weak overlaps between neighboring transitions: $|1\rangle \rightarrow |2\rangle$ with $|2\rangle \rightarrow |4\rangle$; $|1\rangle \rightarrow |2\rangle$ with $|1\rangle \rightarrow |3\rangle$; $|2\rangle \rightarrow |4\rangle$ with $|3\rangle \rightarrow |4\rangle$, respectively. Substituting equation (30) into equation (28), and neglecting small terms and those far from resonance gives

$$U_1(s, T) \approx U_{1ne}(T) + U_{1e}(T)e^{if_1(s)} + U_{12}(T)e^{i(f_1(s)+f_2(s))} + U_{1ee}(T)e^{i2f_1(s)}, \quad (32)$$

where

$$U_{1ne}(T) = \int_0^T C'_0(t_2) \int_0^{t_2} C'''_0(t_1) dt_1 dt_2, \quad (33)$$

$$U_{1e}(T) = \int_0^T C'_0(t_2) \int_0^{t_2} C_1(t_1) dt_1 dt_2, \quad (34)$$

$$U_{12}(T) = \int_0^T C'_2(t_2) \int_0^{t_2} C_1(t_1) dt_1 dt_2, \quad (35)$$

$$U_{1ee}(T) = \int_0^T C'_1(t_2) \int_0^{t_2} C_1(t_1) dt_1 dt_2. \quad (36)$$

The subscript notation of the various amplitudes describes their physical origin. The amplitudes U_{1ne} and U_{1e} correspond to the non-encoded and modulated-by- $\exp[if_1]$ parts of pathway 1, respectively. Only overlaps between neighboring transitions are considered here. U_{1ee} is the part of pathway 1 modulated by $\exp[i2f_1]$ that arises from the overlap between the two transitions of pathway 1 ($|1\rangle \rightarrow |2\rangle$ and $|2\rangle \rightarrow |4\rangle$). The latter overlap (accounted for in the field of equation (30) by the term depending on $C'_1(t)$) causes part of the integral over t_2 in equation (28) to be modulated by $\exp[if_1(s)]$, which combines with the modulation applied to the integral over t_1 (i.e. $\exp[if_1(s)]$) producing the term modulated as $\exp[i2f_1(s)]$ in equation (32). Similarly, U_{12} is the part of pathway 1 modulated by $\exp[i(f_1 + f_2)]$ arising from the overlap between transition $|1\rangle \rightarrow |2\rangle$ (which belongs to pathway 1) and $|1\rangle \rightarrow |3\rangle$ (which belongs to pathway 2). Analogously, we have for U_2

$$U_2(s, T) \approx U_{2e}(T)e^{if_2(s)} + U_{21}(T)e^{i(f_1(s)+f_2(s))}, \quad (37)$$

where

$$U_{2e}(T) = \int_0^T C_2(t_2) \int_0^{t_2} C_0''(t_1) dt_1 dt_2, \quad (38)$$

$$U_{21}(T) = \int_0^T C_2(t_2) \int_0^{t_2} C_1''(t_1) dt_1 dt_2. \quad (39)$$

The amplitudes U_{2e} and U_{21} correspond to the parts of pathway 2 modulated by $\exp[i f_2]$ and $\exp[i(f_1 + f_2)]$, respectively. U_{21} arises from the overlap between the transitions $|1\rangle \rightarrow |3\rangle$ (pathway 2) and $|1\rangle \rightarrow |2\rangle$ (pathway 1). Since the entirety of pathway 2 was encoded, $U_{2ne} = 0$. From equation (31) it follows that

$$|U_{1ne}|, |U_{2e}| > |U_{1e}| \gg |U_{12}|, |U_{21}|, |U_{1ee}|. \quad (40)$$

Substituting equations (32) and (37) into equations (27) and (26) gives the modulated signal

$$\begin{aligned} \langle O(s, T) \rangle &\propto |U_1(s) + U_2(s)|^2 \\ &\propto \text{DC} + U_{1e}U_{1ne}^* e^{i f_1(s)} + U_{1e}U_{2e}^* e^{i(f_1(s) - f_2(s))} + U_{2e}U_{1ne}^* e^{i f_2(s)} \\ &\quad + (U_{12} + U_{21}) U_{1ne}^* e^{i(f_1(s) + f_2(s))} + U_{1ee}U_{1ne}^* e^{i 2 f_1(s)} + U_{2e}^* U_{1ee} e^{i(2 f_1(s) - f_2(s))} + \text{c.c.}, \end{aligned} \quad (41)$$

where DC is the sum of all terms not modulated by the encoding, * denotes complex conjugate, and equation (40) was used to keep only leading-order products of amplitudes in each term. Equation (41) illustrates how the output signal is affected by the encoding: each term is multiplied by a distinct modulating function $h(n_1, n_2; s)$, in accordance with the general analysis of section 2.1. Providing that the set of functions $\{h(n_1, n_2; s)\}$ is orthogonal (which may be arranged, as proven in section (A.1)) and using equation (11), the following projections can be extracted from the observed modulated signal $\langle O(s, T) \rangle$

$$P(1, 0; T) \propto U_{1e}(T)U_{1ne}^*(T), \quad (42)$$

$$P(0, 1; T) \propto U_{2e}(T)U_{1ne}^*(T), \quad (43)$$

$$P(1, -1; T) \propto U_{1e}(T)U_{2e}^*(T), \quad (44)$$

$$P(1, 1; T) \propto (U_{12}(T) + U_{21}(T)) U_{1ne}^*(T), \quad (45)$$

$$P(2, 0; T) \propto U_{1ee}(T)U_{1ne}^*(T), \quad (46)$$

$$P(2, -1; T) \propto U_{2e}^*(T)U_{1ee}(T). \quad (47)$$

Due to the c.c. terms in equation (41), for each projection $P(n_1, n_2; T)$ in equations (42)–(47) there is a projection $P(-n_1, -n_2; T)$ which is equal to $P^*(n_1, n_2; T)$.

From equation (40) it is expected that

$$|P(1, 0; T)|, |P(0, 1; T)| > |P(1, -1; T)|, |P(1, 1; T)|, |P(2, 0; T)| > |P(2, -1; T)|. \quad (48)$$

Ratios of pathway amplitudes can be extracted from the experimental data using equations (42)–(47). In particular,

$$\frac{U_1(T)}{U_2(T)} = \frac{P(1, 0; T)}{P(0, 1; T)} + \frac{P(1, 0; T)^*}{P(1, -1; T)^*} \quad (49)$$

and

$$\frac{U_{1ee}(T)}{U_{12}(T) + U_{21}(T)} = \frac{P(2, 0; T)}{P(1, 1; T)}. \quad (50)$$

In equation (49), we used equation (40) to approximate the total pathway amplitudes as $U_1 \approx U_{1e} + U_{1ne}$ and $U_2 \approx U_{2e}$.

As seen above, U_{12} , U_{21} , and U_{1ee} are measures of transition overlaps. Recall that transitions $|1\rangle \rightarrow |2\rangle$ and $|2\rangle \rightarrow |4\rangle$ belong to pathway 1, and transitions $|1\rangle \rightarrow |3\rangle$ and $|3\rangle \rightarrow |4\rangle$ belong to pathway 2. Larger overlaps are due to wider transitions, dynamically induced by the field $E(t)$ (see section 2.3). The ratio $|U_{1ee}/(U_{12} + U_{21})|$ is larger when the transitions of pathway 1 are broad (increasing their overlap, and hence U_{1ee}) while the transitions of pathway 2 stay narrow (decreasing their overlap with pathway 1's transitions, and hence reducing U_{12} and U_{21}). Consider the frequency–time representation of the applied field $E(t)$. As discussed in section 2.3, a wider transition at a given time t implies that a greater portion of the field's frequency bandwidth is around the transition's center at time t . Thus, the projection ratio $|P(2, 0; t)/P(1, 1; t)|$ provides information about the field's frequency content around the transitions at time t , since it maps the time dependence of pathway 1's transition widths relative to those of pathway 2. This information will be used in section 3 for interpreting optimally controlled dynamics.

2.5. Rabi flopping

Rabi flopping is possible at the laser intensity used in the experiments (see section 3). In the context of population transfer in Rb from state $|1\rangle$ to state $|4\rangle$, Rabi flopping requires at least a fourth-order process, e.g.

$$|1\rangle \rightarrow |2\rangle \rightarrow |1\rangle \rightarrow |2\rangle \rightarrow |4\rangle. \quad (51)$$

A large presence of fourth- or higher-order processes could produce a wealth of high-order projections [16]. This situation was not observed in the experiments, where the projections were limited to second-order (see section 3.5). Higher-order processes can nevertheless perturbatively affect the dynamics dominated by second-order pathways. The effects of flopping can appear in the first- or second-order projections, depending on where the transition frequencies lie in relation to the encoding. For instance, if in the fourth-order pathway of equation (51) all the three transitions $|1\rangle \rightarrow |2\rangle \rightarrow |1\rangle \rightarrow |2\rangle$ were excited by the encoded portion of the field around $|1\rangle \rightarrow |2\rangle$ (i.e. encoded spectral components around 780 nm in figure 1(b)), it would give rise to an extra term in equation (27) modulated by $\exp[i(f_1 - f_1 + f_1)] = \exp[i f_1]$ (see also the definition of composite pathways in section 2.1), which would contribute to the projection $P(1, 0)$. If the first and last of the three transitions $|1\rangle \rightarrow |2\rangle \rightarrow |1\rangle \rightarrow |2\rangle$ were excited by the encoded portion of the field (with the remaining transition $|2\rangle \rightarrow |1\rangle$ being excited by a non-encoded spectral component), this would give rise to an extra term in equation (27) modulated by $\exp[i(f_1 + f_1)] = \exp[i2f_1]$ which would contribute to $P(2, 0)$. Given that the encoded portion of transition $|1\rangle \rightarrow |2\rangle$ was much smaller than its non-encoded part (see

figure 1(b)), the most likely scenario is to have only one encoded field spectral component in $|1\rangle \rightarrow |2\rangle \rightarrow |1\rangle \rightarrow |2\rangle$, which would result in a Rabi flopping contribution to $P(1, 0)$. In summary, as performed in the experiments, we expect Rabi flopping to mainly affect the value of projection $P(2, 0)$ and, more importantly, $P(1, 0)$. As a consequence, Rabi flopping could cause interference-driven variations of $P(1, 0)$ due to the pathway amplitude ratio $|U_1/U_2|$ oscillating as a function of time τ at the Rabi frequency. This was observed experimentally, as shown below. These arguments can be easily generalized to higher than fourth-order pathways. A full delineation of these various Rabi flopping pathways could be obtained, for instance, by a sequence of HE-OD experiments where different portions of the $|1\rangle \rightarrow |2\rangle$ spectral transition bandwidth are encoded separately with the functions f_{1a}, f_{1b}, \dots

3. Experimental implementation

3.1. Experimental setup

The experimental setup is shown in figure 2. HE-OD was applied to a gas phase sample of atomic Rb in a cell at 100 °C. A laser pulse creates excitation into states $|4\rangle$ and $|5\rangle$ (see figure 1(a)). The final population of state $|4\rangle$ relaxes through spontaneous microwave emission to state $|O\rangle$ and subsequently decays back to $|1\rangle$ emitting fluorescence at 421.55 nm. The latter emission was then imaged to an Ocean Optics HR-2000 (400 nm) spectrometer and integrated to become the output signal $\langle O \rangle$, which is proportional to the final population of state $|4\rangle$. The experiments utilized a coherent Ti:sapphire femtosecond laser consisting of a Mira oscillator and a 1 kHz legend amplifier. The amplified pulses had a fluence at the sample spot of $\sim 6 \text{ mJ cm}^{-2}$. The laser spectrum is shown as a solid line in figure 1(b) and had a full width at half maximum (FWHM) of $\sim 40 \text{ nm}$ centered at $\sim 790 \text{ nm}$, corresponding to a transform-limited temporal pulse width of $\sim 30 \text{ fs}$ FWHM. Under these conditions laser-induced ionization of the Rb atoms was negligible. Phase modulation was performed with a 4-f configuration pulse shaper having a liquid crystal display with 640 pixels (Cambridge Research Instruments-Spatial Light Modulator (CRI-SLM)), as shown in figure 2. The phase of $E(\omega)$ was obtained from genetic algorithm optimization of the 421.55 nm fluorescence [17]. The resultant optimal field $E(\omega)$ created quantum dynamics in Rb which was then subject to HE-OD process tomography. Before entering the Rb cell, a small portion of the laser beam was sent to a beta barium borate (BBO) crystal to generate a second harmonic signal, which was also measured in order to monitor the pulse intensity at each truncation time τ .

3.2. Encoding

The phases of the laser spectral components of $E(\omega)$ in the intervals $782.5 \leq \lambda \leq 783.2 \text{ nm}$ and $752.9 \leq \lambda \leq 768 \text{ nm}$ were encoded by adding in $f_1(s)$ and $f_2(s)$, respectively. The encoded positions of the spectrum are marked by orange and pink in figure 1(b). The encoding functions $f_1(s)$ and $f_2(s)$ are of the form defined in section A.1 with $m = 100$, which allows for resolving projections $P(n_1, n_2; T)$ with $|n_1| + |n_2| \leq 5$.

Due to the transition overlaps, the encodings over transitions $|1\rangle \rightarrow |2\rangle$ and $|3\rangle \rightarrow |4\rangle$ also weakly affected their neighboring transitions (see section 2.4). The encoding over $|3\rangle \rightarrow |4\rangle$ approximately covers its entire width. These experimental conditions were taken into account in the theoretical model of section 2.4. The encoding for $|1\rangle \rightarrow |2\rangle$ was located at the right of the

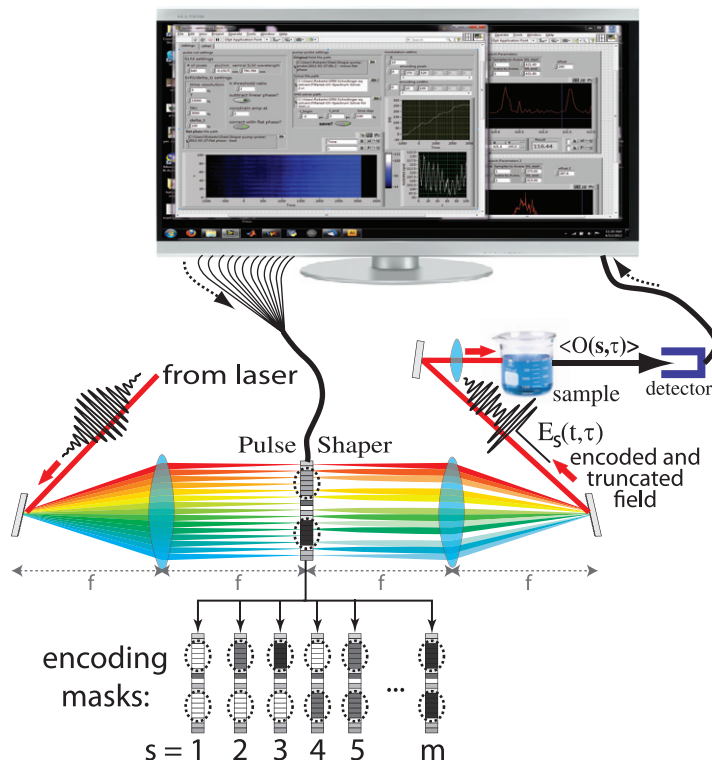


Figure 2. Setup for the time-resolved HE-OD experiments. A shaped laser pulse interacts with a sample, producing an output signal that is fed back to a computer. Information about the participating pathways is obtained through the HE-OD encoding–decoding procedure where special perturbations are added to the field $E(t)$ through encoding masks in the pulse shaper, and the effect of the encoded field $E_s(t)$ on the output signal is decoded to reveal the amplitudes of the various quantum pathways induced by $E(t)$. The lower part of the figure illustrates how the encoding perturbations are implemented by systematically changing the phase of the circled pixels in each mask over a sequence of m separate measurements. To temporally resolve the signal, the SLM mask was further modified to truncate the field $E_s(t)$ at time τ , as described in the text.

transition center (780 nm) in order to reduce encoding in $|2\rangle \rightarrow |4\rangle$ (due to the overlap between $|1\rangle \rightarrow |2\rangle$ and $|2\rangle \rightarrow |4\rangle$).

3.3. Field truncation

The encoded field truncated at time τ , $E_s(t, \tau)$, was generated by cutting the encoded field $E_s(t)$. The appropriate SLM mask was calculated by substituting $E_s(\lambda)$ into equation (23) with a truncation time of $\Delta t = 100$ fs that was much smaller than the temporal width of $E(t)$ which span ~ 4 ps (see figure 3(b)). Since the truncated field depends only weakly on the shape of the spectral amplitude (see section 2.2), $|E(\lambda)|$ was taken as a Gaussian centered at $\lambda_c = 790$ nm and a FWHM of $\Delta\lambda = 40$ nm.

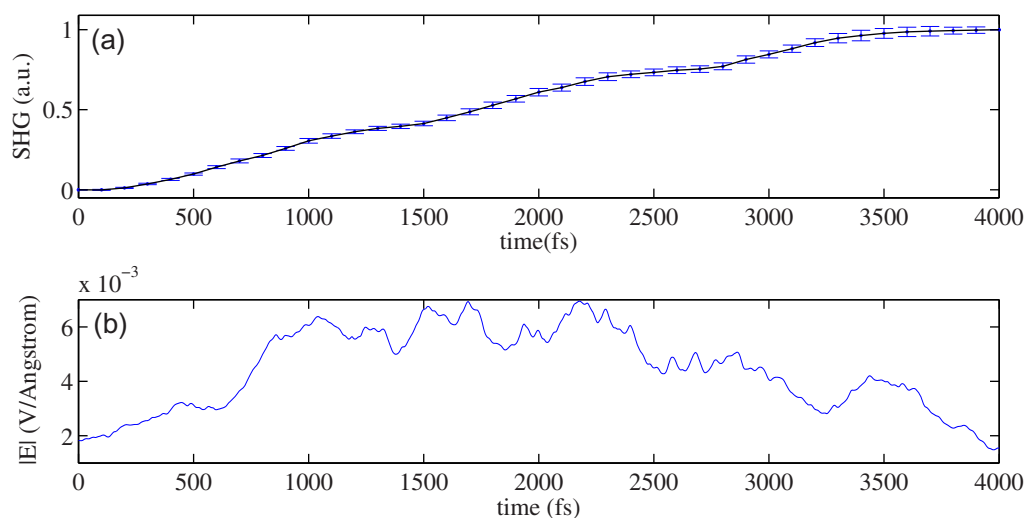


Figure 3. (a) SHG signal as a function of truncation time τ . (b) $|E(t)|$ calculated from the field's spectral profile and the measured fluence.

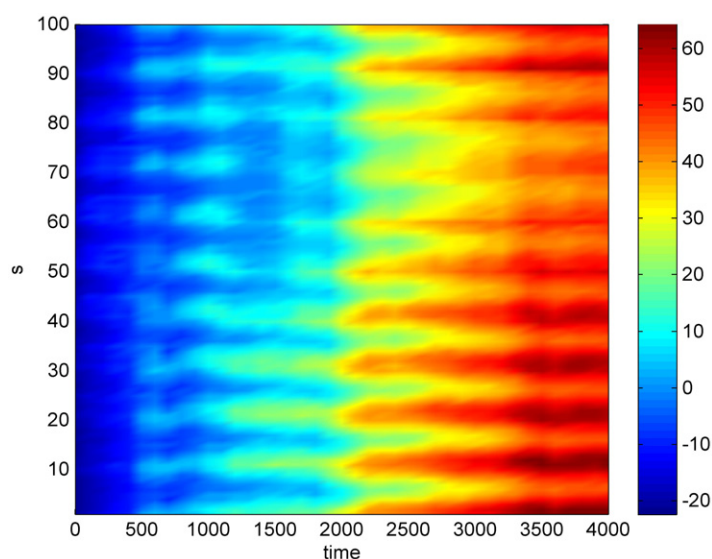


Figure 4. Pseudo-color plot of the time-resolved modulated signal. The ordinate shows the value of the encoding parameter s , whereas the abscissa shows the time τ at which the modulated field $E_s(t, \tau)$ was truncated. The color indicates the value of the measured fluorescence signal. The signal shown here is the average over 14 scans.

As indicated in section 3.1, to monitor the pulse's intensity for every truncation time τ , the SHG signal produced by a portion of the laser beam was also measured, and the SHG(τ) data are presented in figure 4(a). Figure 4(b) shows the pulse's temporal profile $|E(t)|$ calculated from the field's spectral profile $E(\omega)$ and the measured fluence. $|E(t)|$ spans ~ 4 ps, in agreement with the measured SHG(τ), and reaches values of ~ 0.007 V/Å.

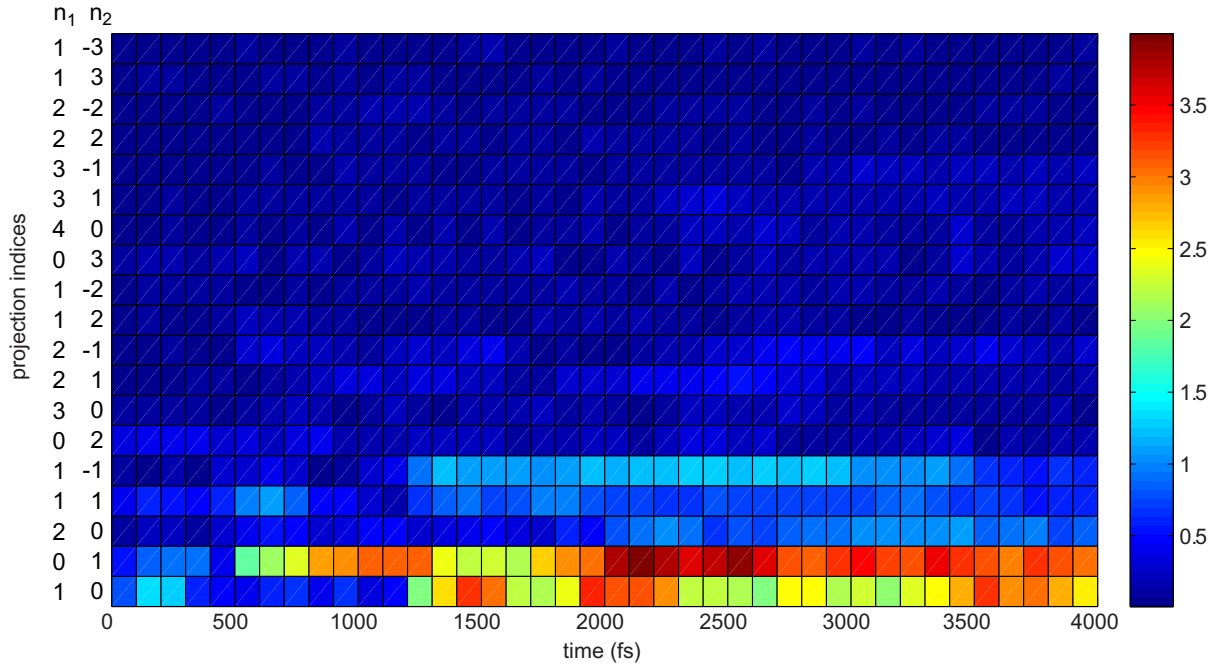


Figure 5. Pseudo-color plots of the projection amplitudes $|P(n_1, n_2; \tau)|$ extracted from the modulated signal. The abscissa is the truncation time τ in fs, and each increment in the ordinate corresponds to a particular projection $|P(n_1, n_2; \tau)|$ whose indices n_1 and n_2 are indicated. The color bar indicates the value of each projection amplitude which was obtained by averaging the projection values extracted from 14 separate measurements of the modulated signal. The set of significant projections indicate that second-order processes are dominant.

3.4. Time-resolved modulated signal

The 421.55 nm Rb fluorescence signal was measured for $m = 100$ modulation points (see section A.1) with the truncation time τ varying from 0 to 4000 fs with a 100 fs step, producing a two-dimensional data set $\langle O(s, \tau) \rangle$. The data set was repeatedly measured 14 times. The average of $\langle O(s, \tau) \rangle$ over the 14 runs is shown in figure 4. The oscillatory behavior of $\langle O(s, \tau) \rangle$ versus s approximately follows the variations over s of the encoding functions $f_1(s)$ and $f_2(s)$. The temporal dependence of $\langle O(s, \tau) \rangle$ shows ~ 500 fs oscillations and a slight time-dependent phase shift (i.e. reflected in the slight non-horizontal features in figure 4) during the first half of the dynamics ($0 < \tau < 2000$ fs).

3.5. Decoding

The modulated signal for each truncation time τ was decoded using equation (11), yielding the projections $P(n_1, n_2; \tau)$. The averages of the projection amplitudes over the total 14 experimental runs are shown in figure 5. Figure 6 displays selected projections. In agreement with the analysis of section 2.4, the projections with the largest amplitude are $P(1, 0; \tau)$ and $P(0, 1; \tau)$ with values well above the noise level. There is also a marginal presence

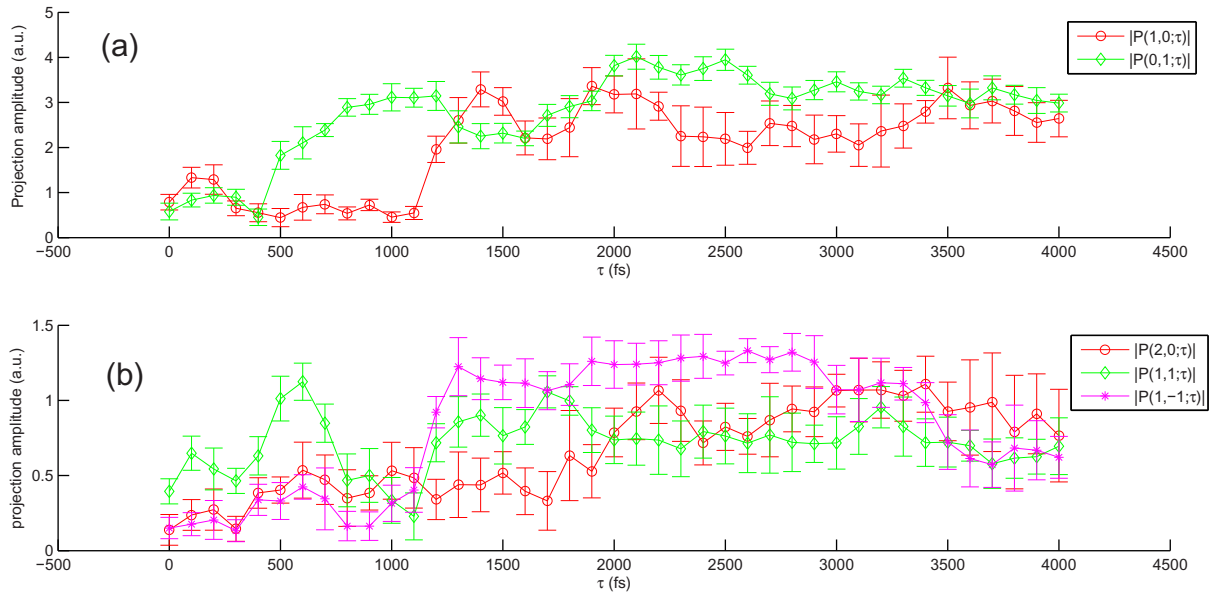


Figure 6. Selected projections versus truncation time τ .

of $P(1, -1; \tau)$, $P(2, 0; \tau)$ and $P(1, 1; \tau)$. The amplitude of projection $P(2, -1; \tau)$ (i.e. the smallest projection predicted in section 2.4) did not exceed the noise level. The absence of projections for $|n_1| + |n_2| > 2$ confirms that second-order processes are dominant and validates the theoretical model of section 2.4, although a higher order Rabi flopping signal shows up through interference (see below).

3.6. Extracted pathway ratios

Two pathway amplitude ratios were extracted from the projections with the help of equations (49) and (50). The results are displayed in figure 7. Oscillations in $|U_1/U_2(\tau)|$ of period $\Delta t \approx 500$ fs are present during approximately the first half of quantum evolution ($0 < \tau < 2000$ fs, see figure 7(a)) as well as in the temporal dependence of some projections (see figure (6)). During the first half of the dynamics, $|U_{1ee}/(U_{12} + U_{21})| < 1$ (except for two noisy points around $\tau = 1000$ fs); whereas, the opposite, $|U_{1ee}/(U_{12} + U_{21})| \geq 1$, takes place in the second half ($2000 < \tau < 4000$ fs, see figure 7(b)).

The results shown in figure 7(a) establish a final pathway ratio of $|U_1/U_2| \sim 5$, implying that pathway 1 is favored over pathway 2 in the optimization of the population transfer to state $|4\rangle$. This value can be understood if the laser spectrum's position with respect to the Rb transitions (see figure 1(b)) is taken into account. According to equations (28) and (29), a rough estimate of the pathway ratio is given by

$$\begin{aligned}
 |U_1/U_2| &\approx \frac{\mu_{12}E(780 \text{ nm}) \times \mu_{42}E(776 \text{ nm})}{\mu_{13}E(762 \text{ nm}) \times \mu_{43}E(795 \text{ nm})} \\
 &\approx \sqrt{\frac{S(780 \text{ nm}) \times S(776 \text{ nm})}{S(762 \text{ nm}) \times S(795 \text{ nm})}} \\
 &\approx 4,
 \end{aligned} \tag{52}$$

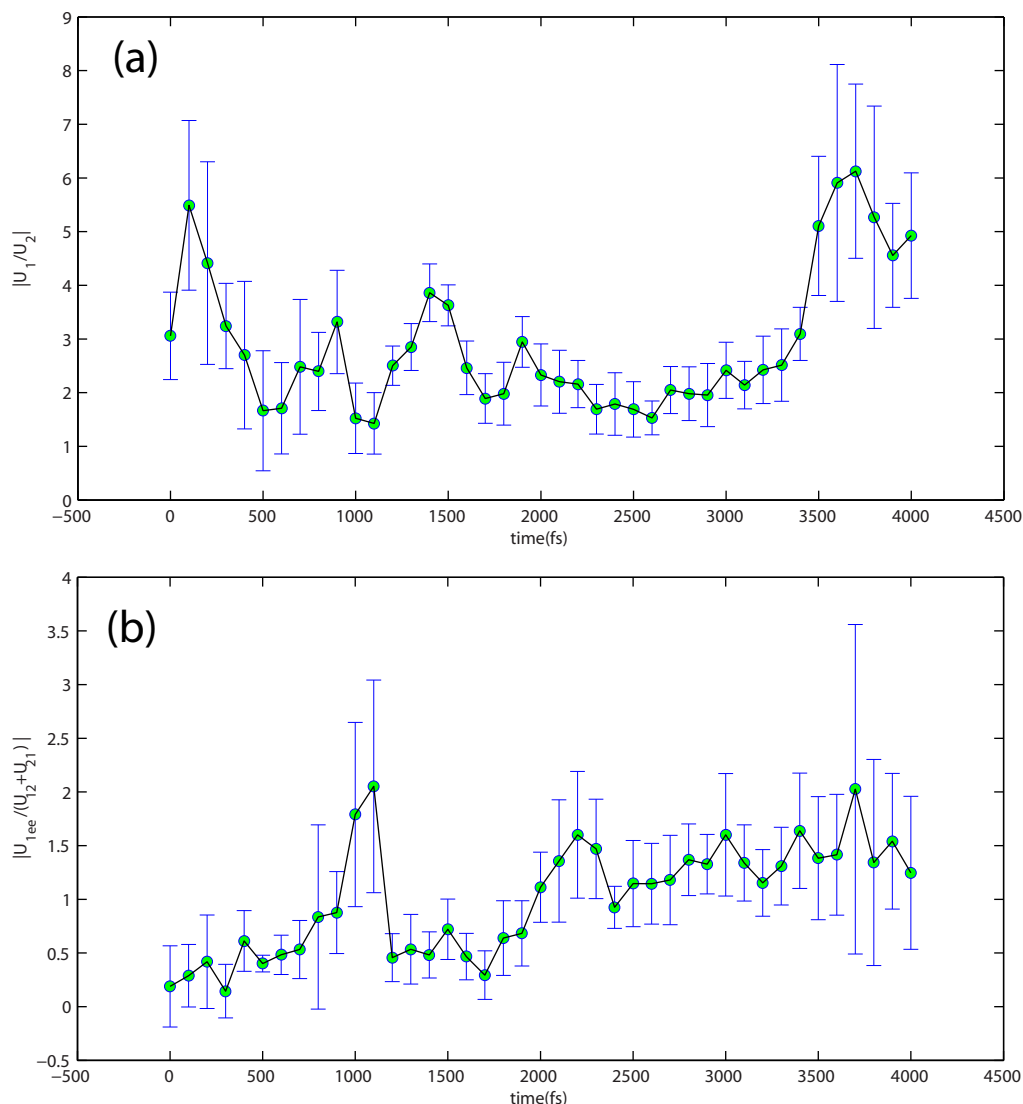


Figure 7. Amplitude ratios $|U_1/U_2|$ (a) and $|U_{1ee}/(U_{12} + U_{21})|$ (b) obtained from the extracted projections and using equations (49) and (50).

where $S(\lambda)$ is the spectral power at wavelength λ , and here we took into account that the Rb dipole moments satisfy $\mu_{12}\mu_{42} \approx \mu_{13}\mu_{43}$. The estimated pathway ratio in equation (52) agrees well with the measured value.

The ~ 500 fs oscillations in $|U_1/U_2|$ (see figure 7(a)) may be due to Rabi flopping. Indeed, Rabi oscillations with a period of $\Delta t \approx 500$ fs and dipole moment $\mu \sim 1 \text{ \AA } e \times \text{ \AA }$ (where e is the electron charge) correspond to a field amplitude of $\sim 0.008 \text{ V \AA}^{-1}$, which is similar to the 0.007 V \AA^{-1} estimated for our experiments (see figure 3(b)). The beats in figure 7(a) can be thought of as an ‘internal’ heterodyne process interfering the Rabi amplitude with the background dominant $|1\rangle \rightarrow |2\rangle \rightarrow |4\rangle$ and $|1\rangle \rightarrow |3\rangle \rightarrow |4\rangle$ amplitudes. Since the field $E(t)$ maximizes the final population of state $|4\rangle$, the temporal structure of $|U_1/U_2|$ reveals the following optimal population transfer mechanism: the first half of the pulse ($0 < \tau < 2000$ fs)

induces Rabi oscillations that are subsequently suppressed by the second half of the laser pulse ($2000 < \tau < 4000$ fs), allowing the population of state $|4\rangle$ to build up.

Further physical insight can be gained from the ratio $|U_{1ee}/(U_{12} + U_{21})|$ since it reflects the applied field's frequency–time content around the transitions (see section 2.4). The evolution of $|U_{1ee}/(U_{12} + U_{21})|$ shown in figure 7(b) demonstrates that for the first half of the pulse (with the exception of two noisy points around $\tau = 1000$ fs) the applied field has less spectral content around pathway 1 than during the second half of the pulse. Focusing on pathway 1 at the end of the pulse increases the final population transfer because pathway 1 is dominant, as was demonstrated above.

4. Future prospects for HE-OD tomography

Based on simultaneously controlling the phases of individual pathways contributing to an observed signal, the HE-OD technique was developed to retrieve quantum pathway amplitudes from a special set of modulation experiments. By combining HE-OD with a laser pulse truncation procedure, time-resolved quantum process tomography was demonstrated on atomic Rb. A fundamental feature of temporally resolved HE-OD is its capability of providing either full or partial process reconstruction. HE-OD is applicable to a broad variety of systems since it relies solely on the system's response to laser pulse phases, and the general laboratory setup does not depend on particular details of the system's Hamiltonian. These attributes make HE-OD a promising tool for investigating quantum dynamics in complex systems relevant to quantum computation, nanotechnology, quantum biology, chemistry, etc. For example, HE-OD has recently been applied to the analysis of laser–plasma interactions during supercontinuum generation [16].

Further applications to complex systems may require simultaneously probing a large number of pathways, scaling up the demand for measurements. Nevertheless, it is possible to reduce the required amount of data in multiple ways: (i) utilizing advanced algorithms to decode the projections [18]; (ii) performing random sampling [12] to take advantage of efficient Monte Carlo integration (projection) of high-dimensional functions; (iii) reducing the complexity of the problem by combining HE-OD with high-dimensional model representation (HDMR) [19]. HDMR is a universal tool for exploring the functional dependencies of observations that draw on large numbers of variables. In particular, HDMR can break down the high-dimensional space of encoding parameters into a natural hierarchy to guide experiments and estimate the outcome of yet unmeasured encoding masks in an iterative manner [19]. Hamiltonian identification [9] can also incorporate HE-OD as an explorative tool for model generation. For a quantum system with known spectral lines (information that can be easily obtained from standard spectroscopy), it is possible to encode the transition frequencies (or portions of their bandwidths) corresponding to the spectral lines, while measuring a suitable output signal (e.g. fluorescence, optical absorption, etc). Decoding the modulated output signal provides a wealth of information that can be used to construct a model of the unknown Hamiltonian. For instance, in this work, from the absence of high-order projections we concluded that the second-order processes were dominant and constructed a physical model that explained the observed set of projections, with higher-order contributions appearing only as modifications of the overall dynamics. The qualitative model can then be used as an input to a quantitative Hamiltonian inversion algorithm again utilizing modulation data. The model itself need not be limited to unitary dynamics. HE-OD experiments can be adapted to the study of open systems or even non-quantum systems, since there is full

freedom in the nature of the physical model underlying the observed projections. In particular, resolving the temporal evolution of the various pathway amplitudes, as demonstrated in this work, could aid in determining the role of decoherence in open quantum systems. We expect that the results reported in this paper as well as on-going developments will make HE-OD an efficient and flexible quantum tomography tool.

Acknowledgments

The authors thank NSF and ARO for financial support.

Appendix

A.1. Orthogonal set of modulating functions

To generate an orthogonal set of modulating functions $\{h(r, q; s)\}$, we begin by sampling an array $\{\phi_j\}$ of regularly spaced phases in the interval $[0, 2\pi]$

$$\phi_j = 2\pi j/R, \quad j = 0, \dots, R-1, \quad (\text{A.1})$$

where R is a positive integer. The encoding functions $f_1(s)$ and $f_2(s)$ are constructed from a Cartesian product of two-phase arrays $\{\phi_j\}$:

$$\begin{aligned} f_1(1) &= \dots = f_1(R) = \phi_0, \\ f_1(R+1) &= \dots = f_1(2R) = \phi_1, \\ &\vdots \\ f_1(m-R+1) &= \dots = f_1(m) = \phi_{R-1}. \end{aligned}$$

And

$$\begin{aligned} f_2(1) &= \phi_0, \quad f_2(2) = \phi_1, \dots, \quad f_2(R) = \phi_{R-1}, \\ f_2(R+1) &= \phi_0, \quad f_2(R+2) = \phi_1, \dots, \quad f_2(2R) = \phi_{R-1}, \\ &\vdots \\ f_2(m-R+1) &= \phi_0, \quad f_2(m-R+2) = \phi_1, \dots, \quad f_2(m) = \phi_{R-1}, \end{aligned}$$

where $m = R^2$.

Substituting $f_1(s)$ and $f_2(s)$, as defined above into the scalar product equation (10), gives

$$\begin{aligned} h(r, q; s) \circ h(r', q'; s) &= \frac{1}{m} \sum_{s=1}^m e^{i[(r-r')f_1(s) + (q-q')f_2(s)]} \\ &= \frac{1}{R^2} \sum_{j,k=1}^R e^{i[(r-r')\phi_j + (q-q')\phi_k]} \\ &= \frac{1}{R^2} \left(\sum_{j=1}^R e^{i(r-r')\phi_j} \right) \times \left(\sum_{k=1}^R e^{i(q-q')\phi_k} \right) \\ &= \frac{1}{R^2} \left(\sum_{j=1}^R e^{i(r-r')2\pi j/R} \right) \times \left(\sum_{k=1}^R e^{i(q-q')2\pi k/R} \right). \end{aligned} \quad (\text{A.2})$$

If $r = r'$ and $q = q'$, then the terms in the summations on the rhs of equation (A.2) are all equal to 1, and therefore $h(r, q; s) \circ h(r', q'; s) = 1$. Suppose instead that $r \neq r'$, then

$$\sum_{j=1}^R e^{i(r-r')2\pi j/R} = e^{i(r-r')2\pi/R} (1 - e^{i(r-r')2\pi}) / (1 - e^{i(r-r')2\pi/R}) = 0,$$

for $|r|, |r'| \leq R/2$. The same holds for q , and q' . We conclude that the set $\{h(r, q; s)\}$ is orthonormal

$$h(r, q; s) \circ h(r', q'; s) = \delta_{r,r'} \delta_{q,q'}$$

for $|r| + |r'|, |q| + |q'| \leq R/2$.

As a consequence of this analysis, note that it may be possible to unambiguously resolve a projection $P(r, q; T)$ from the experimental data only if $|r|, |q| \leq R/2$. Thus, the number of points R of the generating array $\{\phi_j\}$ has to be chosen so that the desired highest-order projections are resolvable.

References

- [1] Banaszek K, Dariano G, Paris M and Sacchi M 1999 *Phys. Rev. A* **61** 010304
- [2] Lvovsky A and Raymer M 2009 *Rev. Mod. Phys.* **81** 299
- [3] Paris M and Řeháček J 2004 *Quantum State Estimation* vol 649, 1st edn (Berlin: Springer)
- [4] Cramer M *et al* 2010 *Nature Commun.* **1** 149
- [5] O'Brien J L *et al* 2004 *Phys. Rev. Lett.* **93** 080502
- [6] Leung D 2003 *Math. J. Phys.* **44** 528
- [7] Mohseni M and Lidar D A 2006 *Phys. Rev. Lett.* **97** 170501
- [8] Shabani A *et al* 2011 *Phys. Rev. Lett.* **106** 100401
- [9] Geremia J and Rabitz H 2002 *Phys. Rev. Lett.* **89** 263902
- [10] Geremia J and Rabitz H 2003 *Chem J. Phys.* **118** 5369
- [11] Mitra A and Rabitz H 2003 *Phys. Rev. A* **67** 33407
- [12] Rey-de Castro R and Rabitz H 2010 *Phys. Rev. A* **81** 63422
- [13] Mitra A and Rabitz H 2008 *Chem. J. Phys.* **128** 044112
- [14] Sakurai J J 1967 *Advanced Quantum Mechanics* 1st edn (Reading, MA: Addison-Wesley)
- [15] Strasfeld D, Shim S and Zanni M 2007 *Phys. Rev. Lett.* **99** 38102
- [16] Rey-de Castro R, Bejot P, Kasparian J, Wolf J and Rabitz H 2012 in preparation
- [17] Judson R and Rabitz H 1992 *Phys. Rev. Lett.* **68** 1500
- [18] Li G, Rey-de Castro R and Rabitz H 2012 *J. Math. Chem.* **50** 1747–64
- [19] Izmailov S, Feng X, Li G and Rabitz H 2012 *J. Math. Chem.* **50** 1765–90